buildings

MDPI

Article

Analysis of a Large-Scale Physical Model of Geosynthetic-Reinforced Piled Embankment and Analytical Design Methods

Jozef Vlček *, Marian Drusa, Filip Gago and Ján Mihálik

Department of Geotechnics, Faculty of Civil Engineering, University of Žilina, Univerzitná 8215/1, 010 26 Žilina, Slovakia; marian.drusa@uniza.sk (M.D.); filip.gago@uniza.sk (F.G.); jan.mihalik@uniza.sk (J.M.)
* Correspondence: jozef.vlcek@uniza.sk

Abstract: The piled embankment represents one of the solutions for the realization of a soil body on a compressible subsoil where extended settlement or insufficient stability threatens the serviceability of related structures. Widely adopted analytical design procedures were analyzed: Marston's formula and Hewlett and Randolph method contained in the British standard BS 8006-1, the German regulation EBGEO and the Dutch regulation CUR 226. Using these recommendations, the theoretical values of the individual parts of the load acting in the embankment and, subsequently, the values of the axial strain or tensile forces in the reinforcement were determined and compared with experimental data obtained from the tests in the large-scale physical model. For the presented case, without subsoil support, CUR 226 with the inverse load, which is recommended in the case of subsoil with low bearing capacity, shows better coincidence with the measured data. Overall, EBGEO and CUR 226 can be considered to be close to the real behavior of the piled embankment. Because of the frequent utilization of geosynthetic reinforcement and possible changes of subsoil parameters during the service life of the piled embankment, a rheological process of its elements should be investigated during the design process.

Keywords: CUR 226; EBGEO; Hewlett and Randolph; Marston; piled embankment; physical model

check for updates

Citation: Vlček, J.; Drusa, M.; Gago, F.; Mihálik, J. Analysis of a Large-Scale Physical Model of Geosynthetic-Reinforced Piled Embankment and Analytical Design Methods. *Buildings* **2023**, *13*, 1464. https://doi.org/10.3390/buildings13061464

Academic Editor: Yong Tan

Received: 25 April 2023
Revised: 1 June 2023
Accepted: 2 June 2023
Published: 4 June 2023

1. Introduction

A soft subsoil with insufficient bearing capacity and deformation characteristics represents one of the common problems in the design of geotechnical structures. Detailed investigation of the subsoil allows a proper decision process to choose the efficient and safe design [1–3]. The piled embankment represents one of the solutions for the realization of a soil body on a compressible subsoil where extended settlement or insufficient stability threatens the serviceability of related structures such as communications, bridges or buildings [4–7]. Other advantages include maintaining restricted deformations, shorter construction time compared to other technologies and the possibility of realization of the construction even in the winter period. The structure typically consists of three basic elements: the piles, the basal reinforcement on the pile caps and the embankment body. The piles fulfill the role of the vertical supporting elements, which allows the transfer of the load over the soil layers with the low bearing capacity to the subsoil with sufficient resistance. Ongoing research allows a better understanding of piled embankment behavior to produce safe and more efficient designs [8].

The creation of arching is an important phenomenon in each piled embankment. The arching effect was defined by McNulty as "the ability of a material to transfer loads from one location to another in response to a relative displacement between the locations. A system of shear stresses is the mechanism by which the loads are transferred" [9]. Clastic material, such as sand, gravel or crushed aggregate, is a common filling material. A simplified approach lies in as assumption of the trap-door effect of unsupported soil mass where stress redistribution occurs [10,11]. However, several studies indicate a more complex behavior where a higher friction angle of the fill leads to the arching effect in the embankment being more prominent [12–15]. The internal friction of the soil can be improved by additional elements such as mixed fibers [16]. The arching development is also governed by the geometric configuration-pile head size and spacing and embankment height [17–20]. A critical height of the embankment, estimated by several authors, defines if partial or full arching will develop (Figure 1). In both cases, the weight of the embankment with the height *H* and the surcharge load on the top of the embankment are divided to load part A directly acting on the pile heads and load part B below the arch acting on the basal reinforcement. The total load on the pile cap is the sum of the load parts A and B (A + B). Component C represents the reaction of the subsoil.

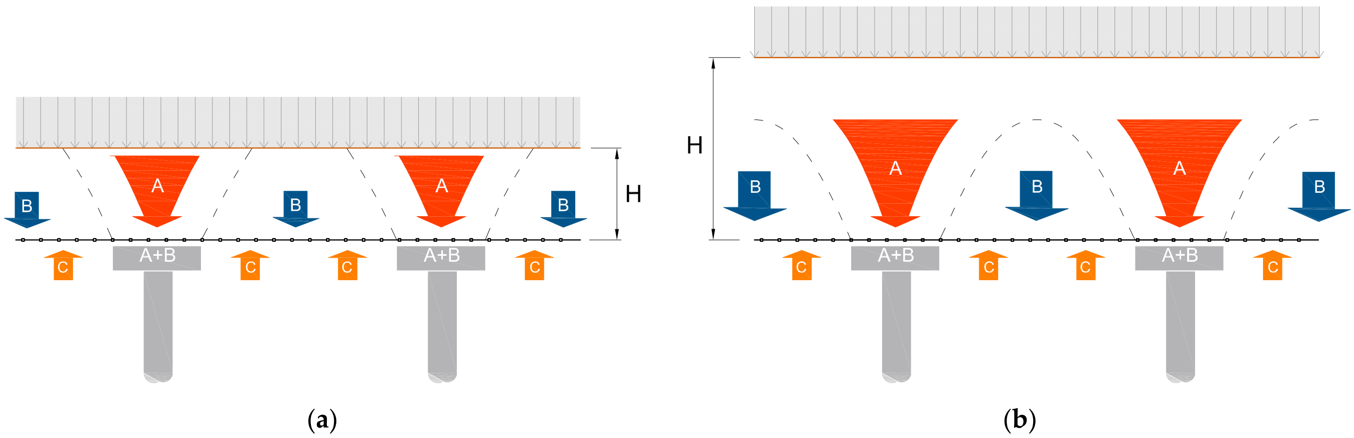

Figure 1. Distribution of the load in the piled embankment: (**a**) partial arching development; (**b**) full arching.

It should be noted that cyclic load can cause stress redistribution because of creep strain and strain softening of granular soils. The stress redistribution at the base of the embankment increases the load acting directly on the pile caps [21,22].

The group of calculation models with a fixed arch shape belongs to the widely used models for the determination of the arching effect. The characteristic feature of these models is the fixed shape of the soil arch. It is mostly a triangular shape with a defined slope from the pile cap edge. The weight of the soil under the triangle is supported by the geosynthetic reinforcement and the subsoil, while the weight of the soil and the load outside this arch is transferred directly to the pile caps. The disadvantage of these models is that they do not take into account the properties of the embankment material such as friction angle or stiffness [23,24].

More advanced equilibrium models—Hewlett and Randolph model, Zaeske model and van Eekelen model—are evaluated in this paper. This category of models is based on the assumption that a stress arc or arches are created between rigid elements (piles or walls) based on the activation of shear stresses. From the balance of the critical part of the arc or of its upper part, the stress acting on the geosynthetic reinforcement and the subsoil is calculated.

Standards and guidelines utilize various methods for arching process estimation. The following methods or guidelines were elaborated on in the study:

- Marston's formula [17]
- Hewlett and Randolph method in British Standard BS 8006-1 [17]
- German guideline EBGEO (Empfehlungen für den Entwurf und die Berechnung von Erdkörpern mit Bewehrungen aus Geokunststoffe) [18]
- Dutch guideline CUR 226 (Report 226 Ontwerprichtlijn paalmatrassystemen) [20]

A detailed characterization of mentioned methods is beyond the scope of this paper, only a brief description is listed below.

Marston's formula was originally derived from field tests carried out on buried pipelines. Jones modified the formula so that it could be applied to a 3D situation, i.e., on the piled embankment. Equations for arching effect coefficients were developed based on embankment height, pile head width, and pile type (embedded or friction piles). According to the geometric configuration, the model distinguishes between two types of the embankment—an embankment with partial or full arching. This condition further affects the load distribution in the embankment. The theory is based on the determination of the uniform vertical load that is carried by the reinforcement between adjacent pile heads [25,26].

The Hewlett and Randolph model represents an alternative solution to the Jones model in BS 8006-1. Hewlett and Randolph derived their theoretical solution for arching based on observations from experimental tests. The tests were carried out without geosynthetic reinforcement. The soil arch transfers most of the load to the pile heads, and the subsoil transfers the load only from the material located under the arch, while the arch has a semicircular shape with uniform thickness. The theory deals with two critical places, the crown of the arch and above the pile heads, in which it is necessary to determine the efficiency E. The efficiency defines the proportion of the weight of the embankment carried directly by the piles [27].

For calculation of the forces in the reinforcement, BS 8006-1 standard assumes the uniform distribution load that is located only in the strips between the pile heads (Figure 2a). The subsoil does not participate in the transfer of the load from the embankment; the load component C is equal to zero. The stiffness of the reinforcing elements is also not included in the calculation of the tensile force or axial strain. To determine the tensile force in the reinforcement, it is necessary to enter the axial strain of the geogrid. This parameter has to be estimated according to the boundary conditions given by the standard.

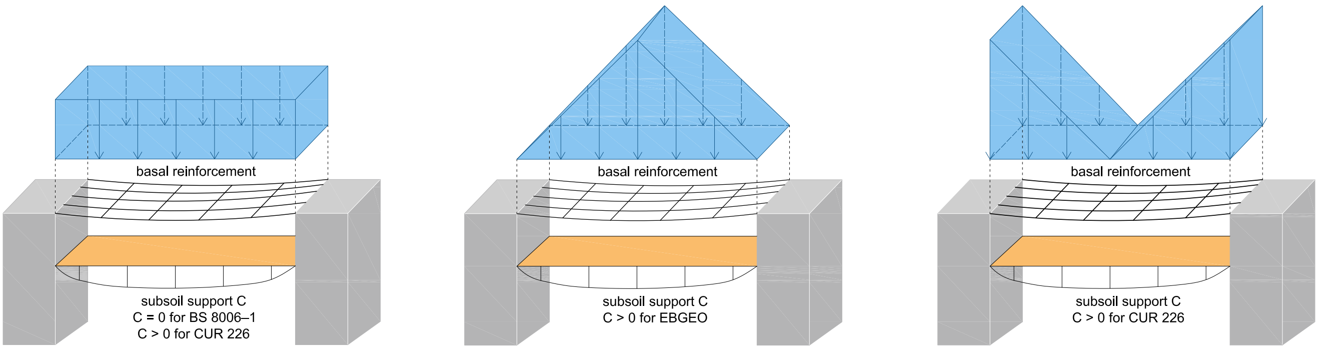

(**a**) (**b**) (**c**)

Figure 2. Load distribution on the basal reinforcement: (**a**) BS 8006-1 and CUR 226 UL; (**b**) EBGEO; (**c**) CUR 226 IL.

The German guideline EBGEO is based on the analytical solution of the stress distribution of the equilibrium model proposed by Zaeske [28]. The verification of the theory is based on laboratory scale models as well as numerical calculations. Zaeske's model assumes the formation of several non-concentric semicircular arches. The upper arch has a radius equal to half of the diagonal axial distance of the piles, and the lowest arch is almost flat, while the radius approaches infinity.

The calculation of the tensile force in the reinforcement for EBGEO assumes the occurrence of a load with a triangular propagation, the influence of which is concentrated in the rhombus area between pile caps (Figure 2b). In contrast to BS 8006-1, the subsoil participates in the load transfer from the embankment. However, the subsoil reaction area is only in the strip between the heads of adjacent piles.

The Van Eekelen model of concentric arches, which is included in the CUR 226 guideline, assumes the creation of multiple arches that are concentric and have a semicircular shape. The geogrid strain is the condition for this behavior. The arching process has several stages. In the initial phase of the geogrid strain, arches are first formed in the area of the pile heads. In subsequent phases, further deformations of the geogrid activate shear stresses on a larger scale, which leads to the connection and formation of arches with the largest radius and then an infinite number of arches of smaller radius between adjacent piles. In the three-dimensional model, these arches are divided into the 3D arches and the 2D arches. The 3D arches are formed in the space between the four piles and thus directly transfer part of the load to that area. The remaining part of the load, which is not transferred to the area between the piles directly, is transferred to the 2D arches as a uniform load using shear stress. Furthermore, this load is transferred through the 2D arches to the pile heads and the geogrid between the piles [20].

The Dutch guideline involves the two calculations of the reinforcement tensile force. The bearing capacity of the subsoil is the decisive condition that determines the propagation of the load acting on the base of the embankment. The first approach includes a situation where the design envisages the support of the subsoil. For this case, CUR 226 recommends using a calculation method that assumes the application of a uniform distribution load, which is further marked as CUR 226 UL (Figure 2a). If the subsoil has a negligible bearing capacity, we can exclude its influence from the calculation. For this situation, CUR 226 recommends choosing a calculation method that assumes the action of an inverse triangular load, which is further designated as CUR 226 IL (Figure 2c).

Experimental studies highlight the variation in arching representation in the design approaches, including the effect of the fill parameters and consolidation or creep of the fill. These factors further influence the stress redistribution in the embankment and are not always adopted by the design methods such as BS 8006-1. Differences were also observed at tensile forces in basal reinforcement. However, load distribution on the reinforcement is in agreement with the analytical solutions when the load is concentrated in the strip on top of and between the adjacent pile heads [29–31]. The numerical approach suggests a more complex view but requires careful approximation and implementation, especially in real-case design, with a higher demand on input data and calculation procedures. It is often used as a verification method for analytical or experimental techniques [32–34]. Evaluation of the application of analytical methods is still necessary because of the aforementioned shortcomings and restrictions of the methods that are widely implemented in the standards and the guidelines [35,36].

This paper is dedicated to the large-scale physical model of the piled embankment without subsoil support with different stiffness of the basal reinforcement. The output of the physical model was compared with the assumptions of the described analytical design methods involved in standards. An evaluation of the physical model, observation instrumentation and experimental procedure for further research were other topics of the paper, which considers the real-case measurements of geotechnical structures [37]. Considering the spatial restrictions of the model, the attachment of the "infinite" reinforcement and related strain gauges using optical fibers were investigated.

2. Materials and Methods

The large-scale physical model was proposed to simulate the behavior of the piled embankment reinforced with the basal geosynthetic reinforcement as a part of the road or railway soil body [38,39]. The model was designed considering the accessibility to the measurement equipment and the scale effect on the measured quantities. We assume the transferability of acquired data to the real scale including the instrumentation of the sensor equipment in the real structure or application [40–43].

The model of the piled embankment consisted of the following elements (Figure 3):

- Supporting piles
- Geosynthetic reinforcement
- Embankment material
- Loading device with the load distribution system

- Supporting plate under the embankment body during the construction.

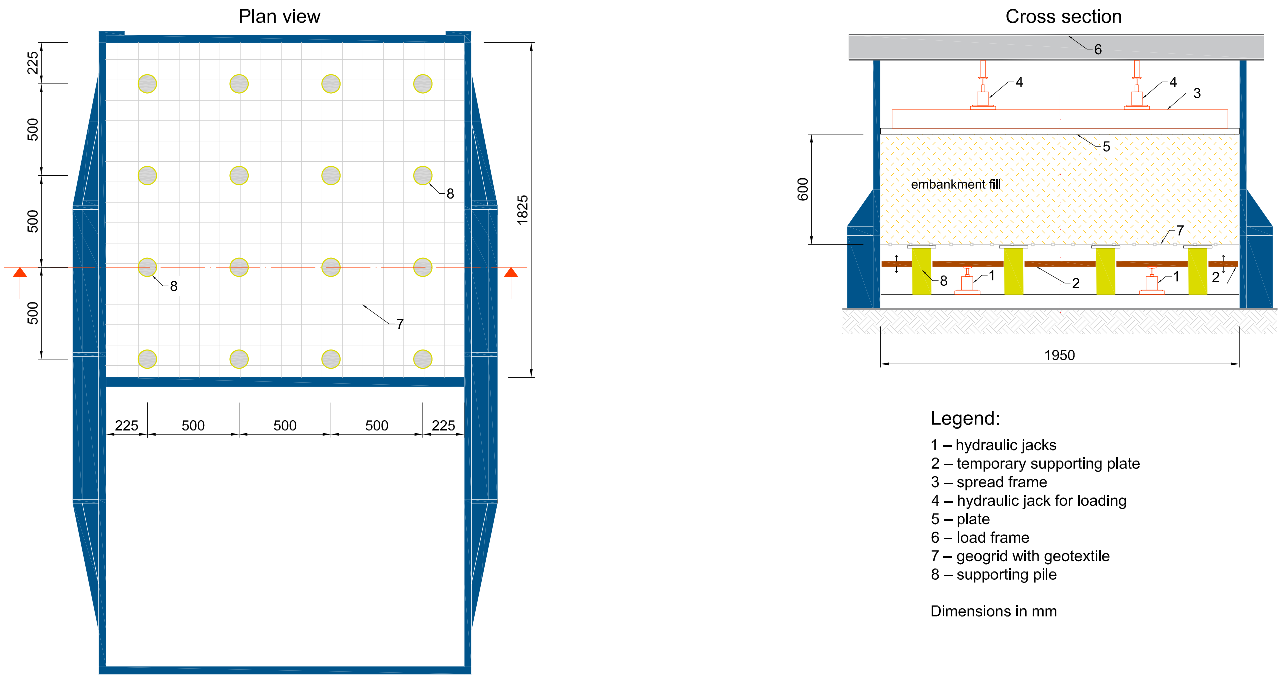

(**a**) (**b**)

Figure 3. The scheme of the physical model of the piled embankment: (**a**) plan view; (**b**) cross-section.

In the proposed configuration, the physical model simulates the central part of the embankment without lateral extrusion. The rigid walls of the model represent the plane of symmetry in the corresponding directions where arching in a particular pile-to-pile box virtually continues beyond the model.

The scale conversion of the model was made based on similar large-scale physical tests considering the usual center-to-center distance of piles between 0.9 and 2.5 m [44]. All the aforementioned model elements were designed at a scale of 1:3; the real structure and their characteristics are described in more detail in the following paragraphs (Table 1).

Table 1. Conversion of physical and geometric parameters of the physical model.

Parameter		Unit	Scale
length	L	m	1:3
area	$A = L \times L$	m^2	1:3^2
stress	$\sigma = F/L$	kN·m^{-2}	1:3
force	$F = \sigma \times A$	kN	1:3^2
tensile stiffness of geosynthetic reinforcement	F/L	kN·m^{-1}	1:3
length	L	m	1:3

The model was constructed in a container with steel walls and a concrete floor, in which 16 supporting piles were placed in a regular pattern. The physical model was designed to focus on load distribution without partial support of the subsoil. For this reason, the model was built without any support except for the support of the plate during construction. At the level of the pile head, a geosynthetic reinforcement was placed, which was anchored to the steel frame. For the embankment body, the granular cohesionless filling material was selected. The uniform surcharge load on the top of the embankment, representing the traffic load, was induced by the load cylinders through the load distribution system.

Within the physical model, the total load is divided into three parts (Figure 1). Part of the load (from the traffic and the weight of the embankment), which is transmitted directly to the piles by the arching effect, will be referred to as load part A. The remaining load B, which acts under the arch and is not directly transferred to the piles by the arching effect, creates a vertical load on the geosynthetic reinforcement. The load part B causes deformation of the geosynthetic reinforcement that generates the tensile forces, which are then transferred to the piles. Thus, piles transfer not only load part A but also load part B to the subsoil. Under normal conditions, part of load C is denoted as the load transferred by the subsoil. In our case, this part of the load was not considered as the physical model was designed to focus on load distribution without the influence of the subsoil.

2.1. Supporting Piles

The piles were manufactured from steel tubes attached to the concrete floor of the container (Figure 3). The diameter of the circular pile head and the cylindrical shaft was 20 cm and 10 cm, respectively. The pile cap diameter is in agreement with the minimal pile cap and pile distance ratio 20 cm/50 cm = 0.40, which is more than 0.15 [44]. For the maintaining space under the embankment for handling and deflection of the geogrid, the height of the piles was set to 30 cm. Geometric parameters of the piles are summarized in Table 2.

Table 2. Geometric characteristics of the piles in the model.

Parameter	Designation	Value	Unit
axial distance of piles	s_x/s_y	0.50	m
clear distance between adjacent pile caps	s_s	0.30	m
diagonal axial pile distance	s_d	0.707	m
pile head diameter	d	0.20	m
pile head area	A_p	0.0314	m^2
area of influence of one pile	A_E	0.25	m^2
equivalent square pile width	a_{eq}	0.1770	m

2.2. Geosynthetic Reinforcement

When selecting a geosynthetic reinforcement, two basic conditions had to be taken into account. The subject of the first condition was to find such a geogrid, whose mechanical parameters would meet the desired 1:3 scale. A second condition was to find such a geogrid whose surface and material would be suitable for the installation of the measurement technology. Usually, high-strength uniaxial geogrids in several layers represent the basal reinforcement. Considering the scale and the symmetry of the model, biaxial geogrids were selected because these are often practically isotropic with relatively low strength and stiffness. Such a configuration simulates the two layers of uniaxial geogrids lying on each other transversally.

Selected Enkagrid MAX geogrids are rigid, biaxial geogrids made of flat extruded polypropylene or polyester bands with the same nominal strength in the longitudinal and transverse directions. In total, five geogrids with different stiffness were used in the experiment. The stiffness of the geosynthetic reinforcement was determined by laboratory load-strain tests provided by the geogrid manufacturer following ISO 10319 (Figure 4) [45]. Geogrid stiffness at 1% strain, in both the longitudinal (machine direction MD) and transversal (cross-machine direction CMD) directions, was used for analytical calculations (Table 3).

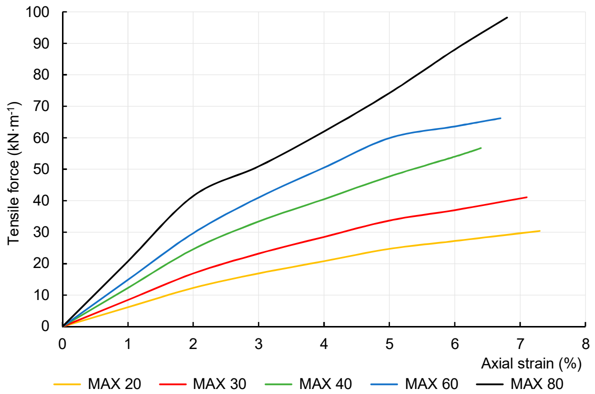

(**a**)

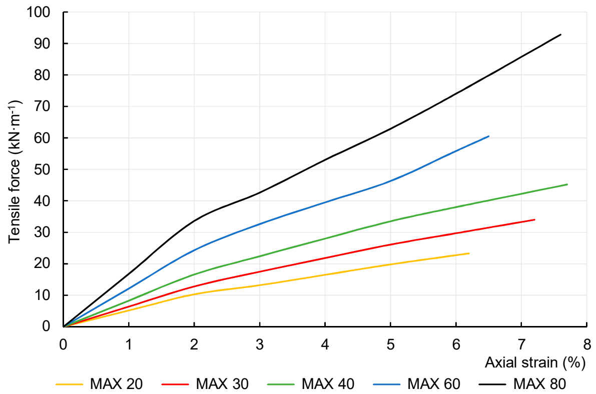

(**b**)

Figure 4. Short-term load-strain properties of geogrids. The number represents the nominal strength of the geogrid in kN·m^{-1} and the geogrid market designation: (**a**) machine direction; (**b**) cross-machine direction.

Table 3. Stiffness of used geogrids at 1% strain.

Geogrid Type	Material	MD Stiffness (kN·m^{-1})	CMD Stiffness (kN·m^{-1})
MAX 20	polypropylene (PP)	615	515
MAX 30	polypropylene (PP)	845	640
MAX 40	polypropylene (PP)	1230	830
MAX 60	polyester (PET)	1485	1215
MAX 80	polyester (PET)	2075	1680

The geogrid was attached to the steel frame simulating the continuity of the geogrid in the real structure together with the anchoring effect in horizontal direction because of friction at the contact of the embankment fill and the reinforcement (Figure 5a) [46]. In that case, the geogrid behaves like an endless strip. The frame and the method of attaching the geogrid are illustrated in Figure 5.

(**a**)

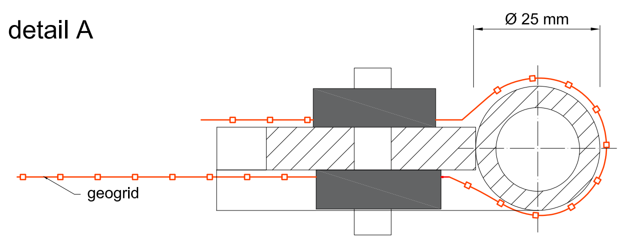

(**b**)

Figure 5. Geogrid installation: (**a**) the frame along with the fixed geogrid placed on pile heads; (**b**) scheme of connection of the geogrid and the frame.

To avoid the overflow of the grains of the fill through the apertures of the geogrid, a low-strength non-woven separation geotextile was applied at the geogrid. In addition, because of no subsoil contact, we assume a lower level of interaction between the geogrid and the fill in contrast with the regular application of such a geogrid in the soil [47].

2.3. Filling Material

Model tests in the centrifuge prove that grains of the embankment material in the scale model must be 20 to 40 times smaller than the distance between adjacent piles [44]. This approach was also applied for the models with the constant gravity conditions. Based on these recommendations, the embankment of the physical model was built from the crushed stone aggregate of a fraction of 0/16 mm (dolomitic limestone). The required parameters of the embankment material were determined based on a series of laboratory tests:

- Sieve analysis (Figure 6a)
- Direct shear box test for normal stresses of 25, 50, 75 and 100 kPa (Figure 6b). Stress levels were selected following assumed vertical stresses in the model.
- The hole test for determination of bulk density of compacted material ρ_d
- Minimal and maximal bulk density test ρ_{min} and ρ_{max}

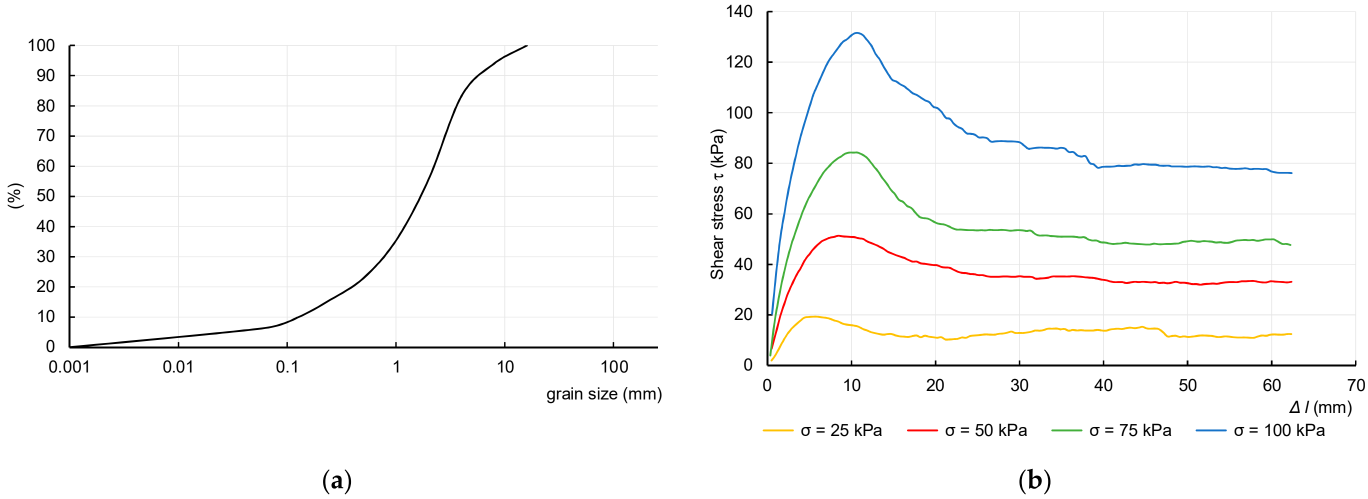

Figure 6. Laboratory tests of the fill: (**a**) sieve analysis; (**b**) direct shear box test propagation for various normal stresses σ as a function of the box displacement Δl.

Parameters of the fill derived from the performed tests are summarized in Table 4.

Table 4. Parameters of the fill.

Parameter	Designation	Value	Unit
classification	S3 = S-F	sand with fine soil	
minimal unit weight	ρ_{min}	1829	kg·m^{-3}
maximal unit weight	ρ_{max}	2186	kg·m^{-3}
friction angle	φ	50.2	degrees
cohesion	c	0	kPa
unit weight of the fill	ρ_d	2075	kg·m^{-3}

The embankment construction procedure was the same for each test. The soil body was built in several layers until it reached the required height of 0.60 m. The embankment material was spread in 15 cm thick layers, which were then evenly compacted by a hand-held circular hammer (Figure 7a).

(a) (b)

Figure 7. Preparation of the fill: (**a**) compaction of the fill; (**b**) the fill after compaction.

Analytical methods assume the development of full arching above pile caps when the embankment reaches critical height H as described in Table 5. Following the recommendations, the embankment was designed with full arching.

Table 5. Minimal embankment height for selected standards and guidelines for full arching.

Minimum Height of Embankment for Creation of Full Arching According to:	Criteria	Theoretical Value for the Model (m)
BS 8006-1	$H \geq 1.4(s_x - a)$	0.45
EBGEO	$H \geq 0.8(s_d - a)$	0.41
CUR 226	$H \geq 0.66(s_d - a)$	0.33

2.4. Load Transfer

In the case of a real structure, the load in the embankment can be static and dynamic. The static load consists of the weight of the embankment body and the weight of the permanent structures. The dynamic load is mainly induced by the traffic load.

Based on the study of Heitz, which describes experimental measurements with a dynamic load, it can be concluded that static and dynamic loads affect the load distribution in a different way [48]. The degree of reinforcement is an important factor. Depending on the reinforcement, the dynamic load can support or, in turn, disable the formation of arches in a piled embankment.

The dynamic load from traffic was simulated as a quasi-static uniform load in the model. The total load at the basal reinforcement of the physical model consisted of two components:

- Load component from the weight of the embankment material
- Load component that has been transferred to the embankment construction as a uniform surcharge load

The additional quasi-static load was applied on top of the embankment by using four hydraulic cylinders. The cylinders first carried the point load into the steel frame and then into the spread plate so that the load on the surface of the embankment was uniform (Figure 8). The measurement and regulation of the load were carried out using an oil pressure sensor, which was part of the hydraulic system. During the experiment, the surcharge load ranged from 0 to 300 kN or 0 to 92.6 kPa, respectively.

(a) (b)

Figure 8. Load transfer system: (**a**) steel frame for load distribution; (**b**) hydraulic load cylinders attached to the frame.

2.5. Supporting Plate

The supporting plate located below the basal reinforcement had two features in the model. The first function was to allow the compaction of the fill in the process of construction. The second function was the possibility of its vertical displacement (lowering below the level of the basal reinforcement) to simulate the complete loss of the bearing capacity of the subsoil (Figure 9).

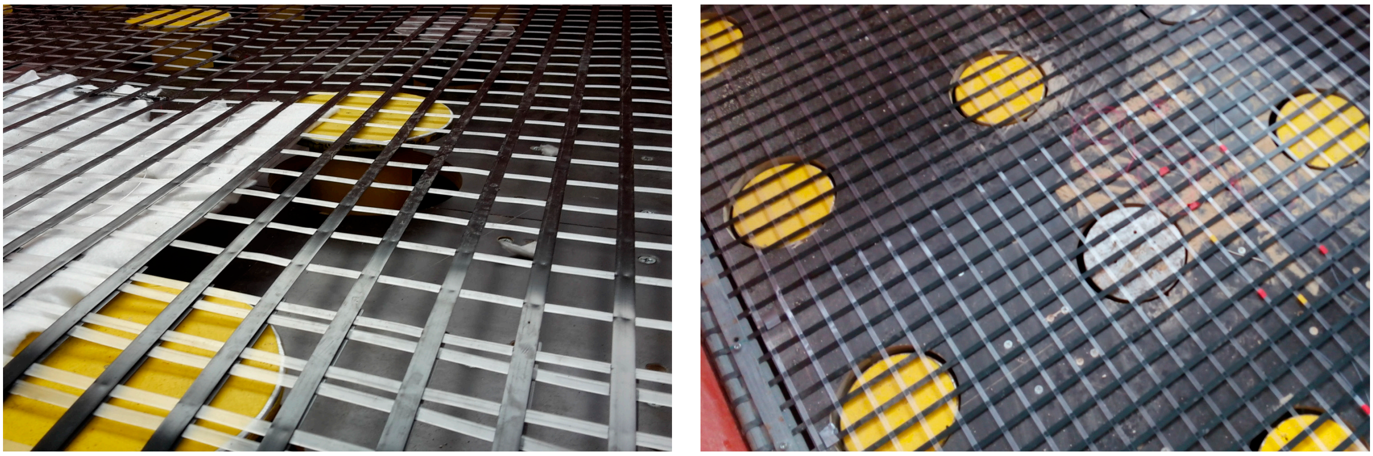

(a) (b)

Figure 9. Supporting plate: (**a**) before lifting; (**b**) after alignment for fill spreading and compaction.

2.6. Measurement Equipment and Test Procedure

The summary of all measurement devices used in the physical model is displayed in Figure 10 and Table 6. The observation was aimed at the arching investigation with the following transfer of the load to the piles and the reinforcement with the measurement of the pile load by using force transducers and the geogrid strain and deflection by using Fiber Bragg Grating sensors (FBG sensors) and potentiometric track sensors.

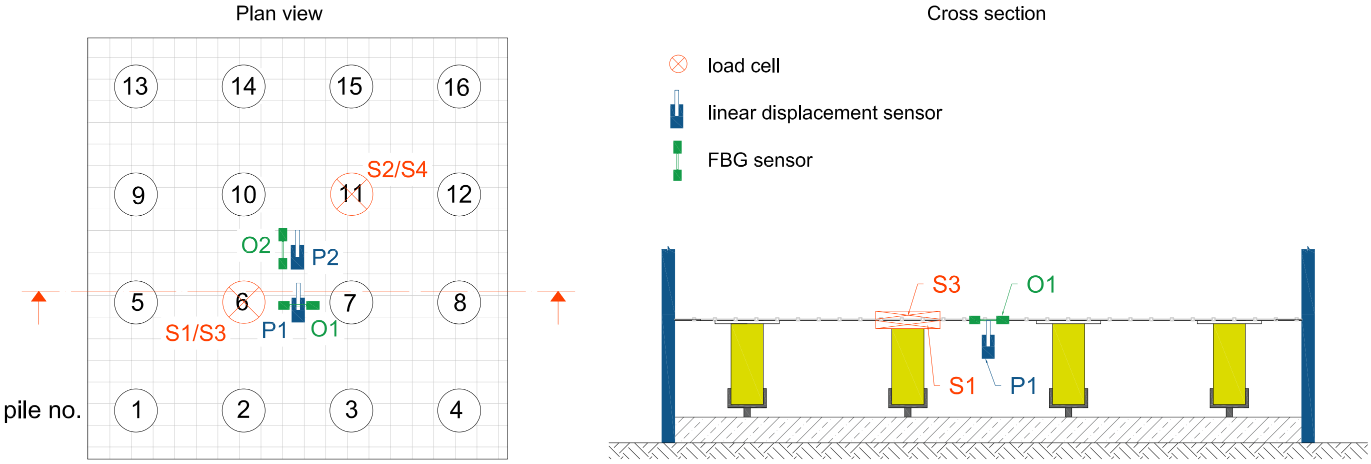

(a) (b)

Figure 10. Measurement instrumentation: (**a**) plan view scheme; (**b**) cross-section.

Table 6. Overview of the measurement equipment in the physical model.

Measurement		Equipment	Unit
vertical pile load	load part A + B (S1, S2)	force transducer based on strain gauges	kN
	load part A (S3, S4)		
axial strain of geogrid	O1, O2	Fiber Bragg Grating (FBG) sensors	- or %
deflection of geogrid	P1, P2	potentiometric track sensor	mm

Each test consisted of the following steps:

- Attaching the geogrid to the steel frame.
- Installation of optical sensors to required positions on the geogrid (marked O1 and O2).
- Placing a supporting plate, simulating a temporary rigid subsoil, into the initial position at the level of the pile heads to form a flat surface.
- Placing the first set of strain gauges (marked S1 and S2) on the piles.
- Placing the frame together with the geogrid into the model. Installing the sensors to measure the vertical position of the geogrid (marked P1 and P2).
- Covering of the geogrid by a separation geotextile.
- Placing of the second set of strain gauges (marked S3 and S4). The second set of sensors is located just above the first set of sensors but above the geogrid and the geotextile.
- Setting the strain gauge force sensors to "zero state".
- Construction of the embankment to the required height of 0.60 m. The spread plate was placed along with the steel frame on the surface of the embankment. The placement of four load cylinders followed.
- Lowering of the supporting plate—this step represents a loss of bearing capacity of the subsoil and was followed by the application of the surcharge load. The loading consisted of 6 stages: 0 → 50 → 100 → 150 → 200 → 250 → 300 kN. At each stage, a load with corresponding intensity was applied until attenuation of observed quantities occurred. The unloading phase was performed in the following stages: 300 → 250 → 200 → 150 → 100 → 50 → 0 kN.

2.6.1. Load in the Embankment

Because of the absence of the subsoil, the load in the embankment was divided into two parts:

- Load part A transferred directly to the piles.

- Load part B transferred through reinforcement to the piles.

Load part A, as well as load part B, were measured by force transducers based on strain gauges adjusted to be able to measure the load from the same area as the pile head. For verification purposes as well as for correction of possible measurement errors, two measuring points were selected at piles No. 6 and No. 11 (Figures 10 and 11). The resulting load is the average of these two measuring points. The strain gauges S3 and S4, located above the geosynthetic reinforcement, measured the load part A. The strain gauge S1 and S2, located directly on the pile head under the geosynthetic reinforcement, measured the sum of load parts A and B. Load part B was determined as B = (A + B) − A.

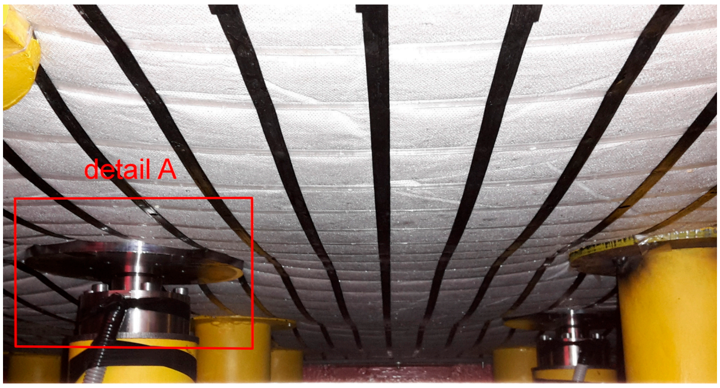

(**a**)

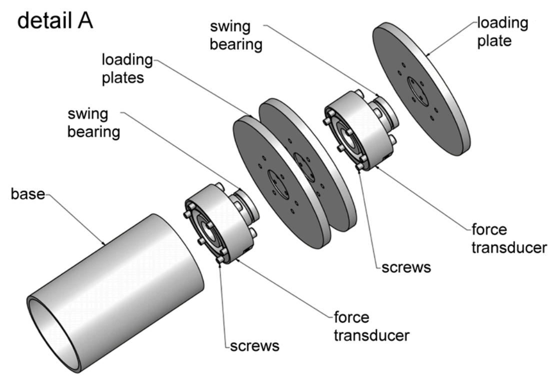

(**b**)

Figure 11. Transducers for pile head load measurement: (**a**) view of the geogrid lying on the pile caps and position of S gauges at the pile cap (detail A); (**b**) pile head with force transducers.

The force transducers were placed between the steel plates to ensure uniform load distribution. For this reason, the pile head for force measurement was also manufactured with swing bearings to avoid the concentration of the load to a certain area of the pile head.

2.6.2. Axial Strain of the Geogrid

Tensile force in the reinforcement is the required output, but direct measurement has to be done by the transfer of the recorded geogrid strain to the tensile force by using the geogrid stiffness in the corresponding strain interval. The measurements of strain were made using sensors based on Fiber Bragg Grating technology (FBG sensors) at the points indicated as O1 and O2 (Figures 10 and 12). The sensor O1 was situated in the strip between the adjacent piles where the major load is assumed according to the studies [13,14] and [49–51]. The sensor O2 was placed on the diagonal between the piles.

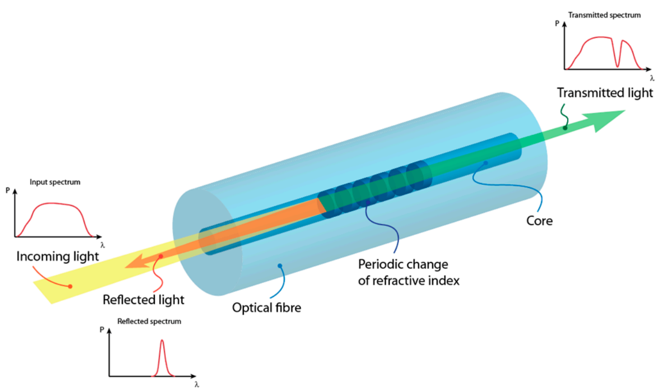

(**a**)

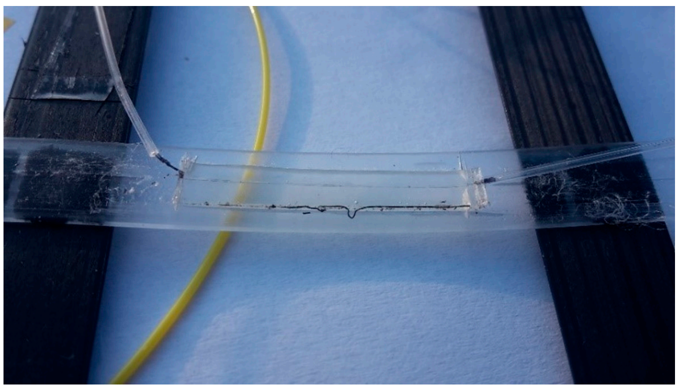

(**b**)

Figure 12. Transducers for measurement of the axial strain of the geogrid: (**a**) the principle of FBG sensor functioning in the spectral region; (**b**) FBG sensor installed on the geogrid.

The principle of FBG sensors is based on Fresnel diffraction (Figure 12a). Propagating optical radiation can be refracted and reflected at the interface between two media with different refractive indexes [52,53]. Fiber grids act as radiation reflectors for specific (required) wavelengths to ensure compliance with the phase adaptation condition. Other (undesired) wavelengths are only slightly affected by the Bragg grid.

2.6.3. Vertical Deflection of the Geogrid

To measure the vertical deflection of the geogrid, potentiometric track sensors were installed below the basal reinforcement. The measurement was carried out at the points indicated in the diagram as P1 between adjacent pile caps and P2 on the diagonal between the piles (Figure 10).

3. Results

Experimental measurements made on the physical model were focused on several areas:

- The redistribution of the load between the pile heads and the remaining part of the basal reinforcement.
- The influence of the stiffness of the reinforcement to form the arches in the embankment or the load distribution within the embankment.
- The comparison of the measured values with the theoretical assumptions of individual standards or regulations.

The experiment consisted of five complete tests with a different stiffness of reinforcing geogrids in each of the tests and the same boundary conditions. For comparison of measured and calculated results, the four analytical models described above were implemented.

For reference of the graphical representation of the results, a force per pile Q_p was introduced. This value is obtained as a ratio of the total vertical stress including the weight of the embankment and the surcharge load and the influence zone A_E around a pile.

3.1. Load Distribution

Because of the absence of the subsoil, the total load was divided into two parts: load part A and load part B (Figure 13). The propagation of the particular load part related to the Q_p value is plotted for each installed geogrid type.

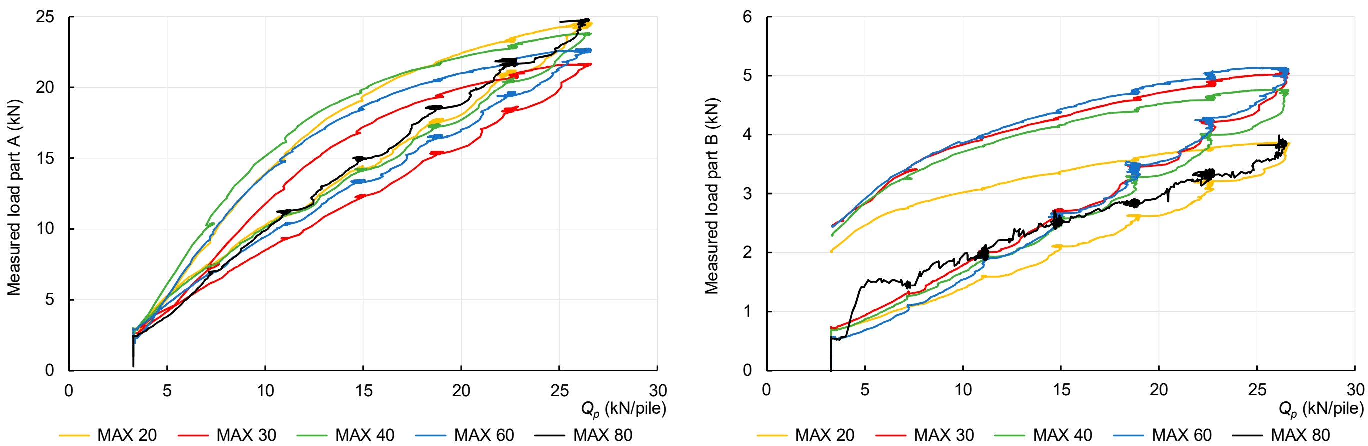

(**a**) (**b**)

Figure 13. Measured load in the model for various geogrids: (**a**) the load part A; (**b**) the load part B.

No trend is observed in the effect of the geogrid stiffness on the arching process, i.e., load redistribution into parts A and B, which is in agreement with other studies [13,14]. The dispersion of the curves can be explained by the uncertainties in the model construction and data recording and interpretation.

Figure 14 demonstrates the comparison of measured and calculated load parts A and B for utilized geogrid types and analytical solutions. The curves for measured values represent the envelope of the final load obtained at a particular loading stage of the corresponding test, and they proved that there was no influence of the reinforcement stiffness on the arching process.

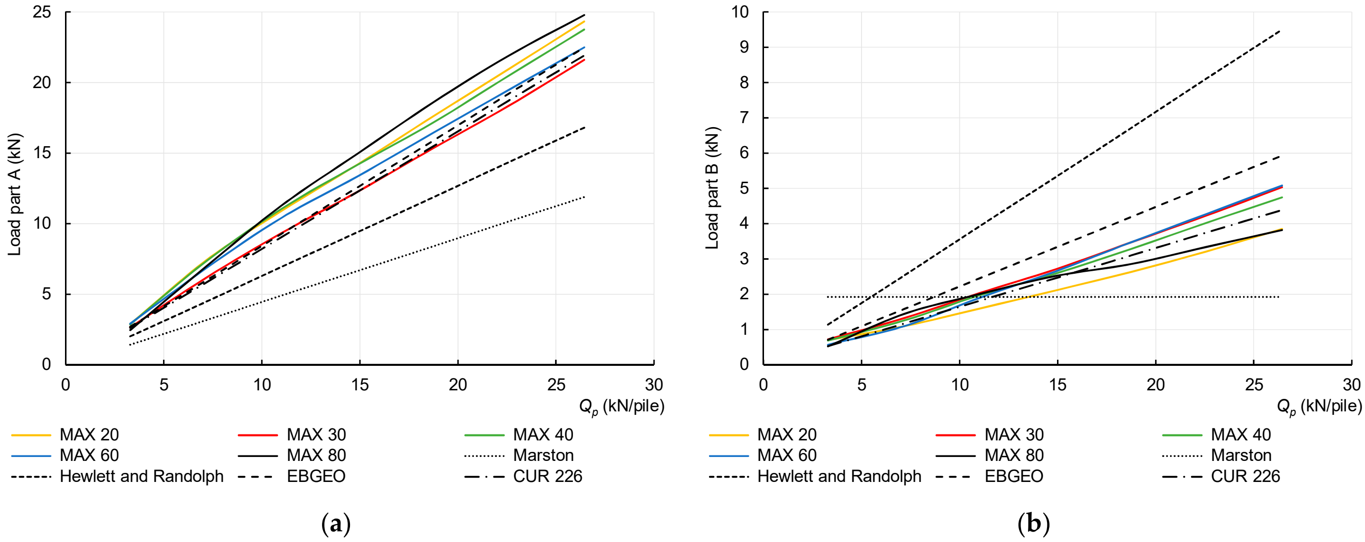

Figure 14. Comparison of measured and calculated load parts A and B: (**a**) load part A; (**b**) load part B.

EBGEO and CUR 226 report the best results in both cases. However, EBGEO shows a slight overestimation of the values of the load part B. On the other hand, both approaches included in BS 8006-1 standard significantly underestimate the load part A, and Hewlett and Randolph method overestimates the B values by a large margin. Marston's theory is restricted in the calculation of the load part B when there is no increase of the load acting on the reinforcement with increasing total load, and the prediction of the B values is vastly unreliable. This imperfection of the approach is based on the optimistic premise that assumes that after the creation of the full arching (condition $H \geq 1.4\ (s - a)$), all the additional load is transferred through the arch directly to the pile heads. The load component B acting on the reinforcement between the pile heads then remains constant regardless of the magnitude of the additional load. It should be noted that this imperfection does not arise in a design meeting the condition of $0.7\ (s - a) \geq \mathrm{H} \geq 1.4\ (s - a)$, i.e., for the embankment with partial arching formation.

The alternative model of Hewlett and Randolph belongs to a group of equilibrium models where such a situation cannot occur. Although the Hewlett and Randolph method assumes a larger load component B, it suggests a similar cumulative load on the pile head as EBGEO or CUR 226.

3.2. Axial Strains and Forces in Reinforcement

Envelope curves for geogrid strain at the measurement points O1 and O2 for a particular geogrid type are plotted in Figure 15.

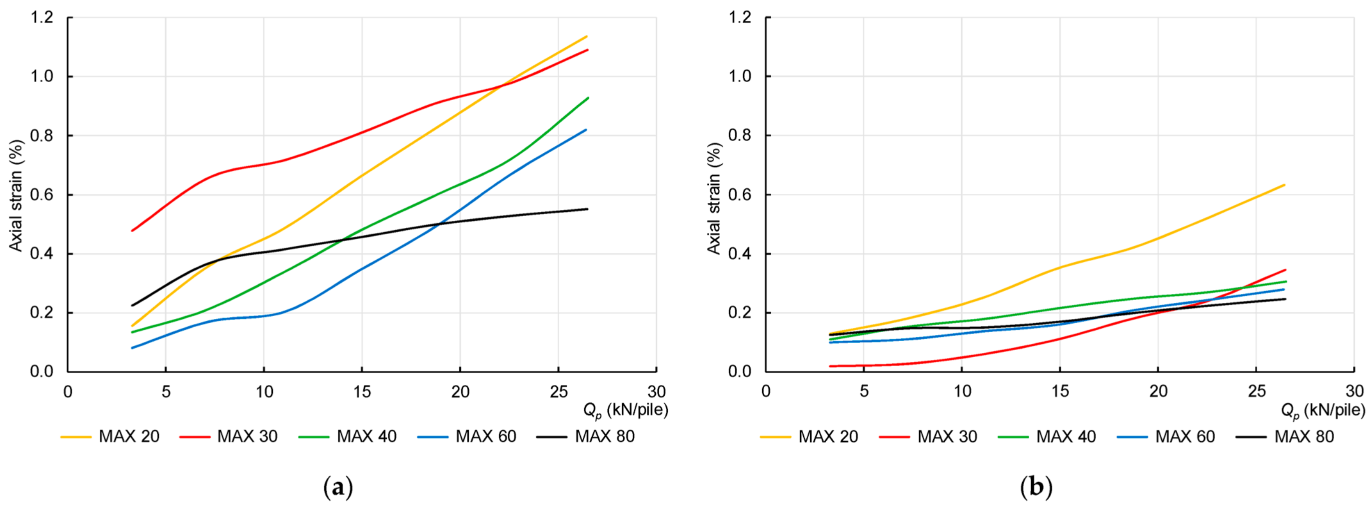

Figure 15. The measured strain of the geogrid in the model: (**a**) the position O1; (**b**) the position O2.

No general trend can be derived from the results since there is no direct proportion between the geogrid stiffness and the related strain. This supports the findings of no influence of reinforcement stiffness on the arching process. Curves are more scattered at the point O1 between adjacent piles where also larger strain values are observed as assumed in the studies [10,12,13,54]. The strain on the diagonal between the piles at point O2 reaches roughly half the value of the strain at point O1. Differences in the curve position and propagation may be attributed to the imperfections of the model and measurement instrumentation and procedure.

The measured strain of the geogrid material was utilized as an input parameter for the determination of the tensile forces by multiplying by a secant stiffness. The stiffness was derived from the load-strain geogrid charts for the 0–1 % strain region, which was confirmed by the experimental outputs.

Figure 16 shows a comparison of the tensile forces in the reinforcement, which is a reaction to the action of the load part B. Theoretical solutions overestimate the tensile force, while the Hewlett and Randolph method is proven to be the least economical. The recommendation in this case is up to 3.8 times higher than the measured value at the last step. Theoretical forces calculated by other guidelines are 1.5 to 2.6 higher than the measured ones, while CUR 226 IL with the inverse reinforcement load shows the smallest deviation—1.5 to 1.9 times the measured value.

3.3. Vertical Deflection of the Geogrid

Despite the obvious difference in the geogrid strain between the adjacent piles and on the diagonal, vertical deflection of the geogrid does not show any significant relation to that behavior (Figure 17). The curves are scattered, and no influence of the geogrid stiffness can be observed. The envelope zone around the curves is very similar for both of the measurement points P1 and P2.

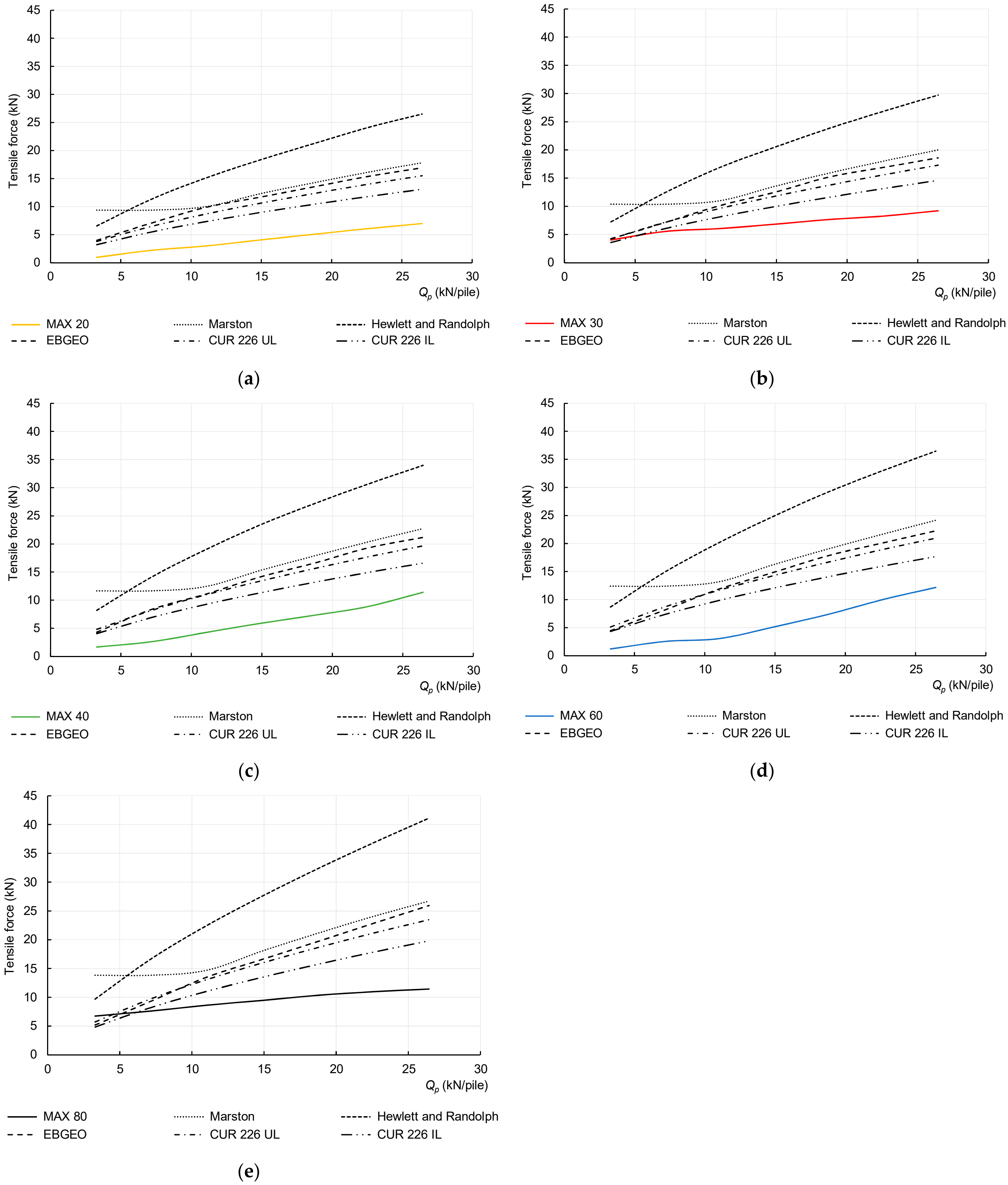

Figure 16. Comparison of measured and calculated tensile forces in the reinforcement: (**a**) the model with Enkagrid MAX 20 geogrid; (**a**) the model with Enkagrid MAX 20 geogrid; (**b**) the model with Enkagrid MAX 30 geogrid; (**c**) the model with Enkagrid MAX 40 geogrid; (**d**) the model with Enkagrid MAX 60 geogrid; (**e**) the model with Enkagrid MAX 80 geogrid.

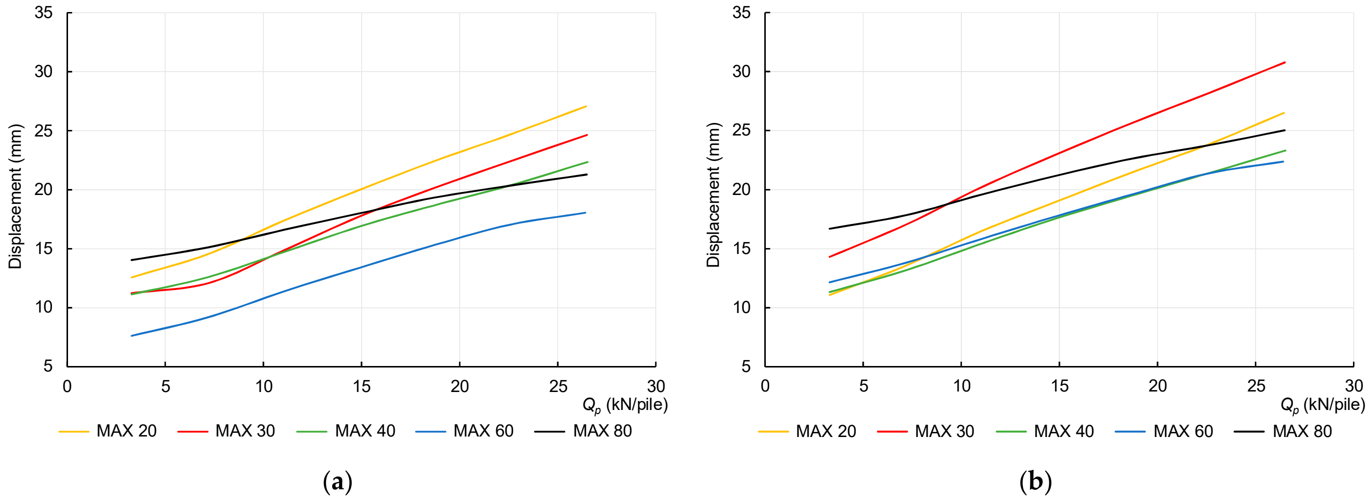

Figure 17. Measured deflection of the geogrid in the model: (**a**) the position P1; (**b**) the position P2.

4. Discussion

Realized measurements on the physical model did not show differences in load distribution between particular reinforcement types. This can be interpreted as the stiffness of the geogrid having no effect on the distribution of the load in the embankment or on the arching development. One of the possible explanations is the assumption that a relatively small strain of the reinforcement and the following deflection is enough to achieve the maximum effect of the arching mechanism.

Marston's formula in BS 8006-1 standard used for determining the load part A underestimates its value. The same can be concluded in the case of load part B when, under certain conditions, a constant load on the reinforcement is considered, regardless of the surcharge intensity. This imperfection is based on the optimistic assumption that after a full arch is created in the piled embankment, all additional loads will be through the arch transferred directly to the pile heads.

The Hewlett and Randolph model also underestimates part of the load that directly acts on the pile head. On the contrary, in the case of the part of the load acting on the reinforcement between the pile heads, the values are overestimated. Although the model assumes a larger load part B component and a smaller load part A component relative to the real measurements, it cumulatively suggests the same load per pile head as EBGEO or CUR 226. However, concerning the outputs of the physical model, it can be concluded that the Hewlett and Randolph model leads to a design that is on the safe side.

The design approach in BS 8006-1 standard does not take into account the reaction of the subsoil or the stiffness of the geogrid. In order to calculate the forces in the reinforcement, an axial strain has to be initially estimated. In the standard, only basic guidance is mentioned. Therefore, the use of this regulation requires certain knowledge about load distribution in real structures.

The comparison of measured and calculated load parts A and B is plotted in Figure 18. Because analytical methods do not take into account the reinforcement stiffness and the physical modelling proved that the stiffness does not affect the arching mechanism, calculated values are rendered against all of the measured forces. A linear trend line was constructed for each analytical method. All the regressions show good alignment with a high coefficient of determination R^2 except Marston's theory at load part B, where this quantity is constant for the embankments with full arching. A 45-degree line represents the ideal course of the regression line. EBGEO and CUR 226 report the best convergence of the results with the deviation of 6.5 and 8.9 % at load part A and 3.8 and 28.8 % at load part B, respectively.

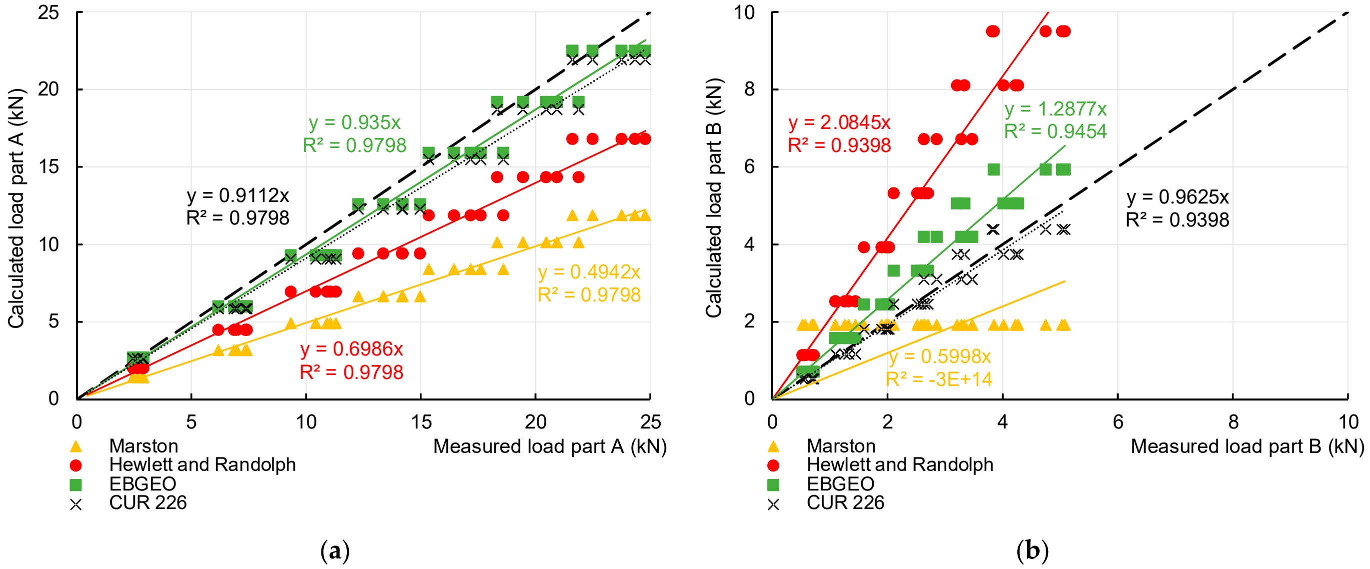

Figure 18. Regression analysis of the analytical methods. The dashed line represents the 45-degree line: (**a**) load part A; (**b**) load part B.

Unlike BS 8006-1, EBGEO and CUR 226 regulations allow us to directly determine the reinforcement strain to calculate the tensile force. The performance of the methods is evaluated in Figure 19. Regression of the plot of measured/calculated strains has a coefficient of determination at 0.8, which is lower than in the case of loads acting on the pile heads. The deviation from the ideal 45-degree line is 100 to 110 % in the case of EBGEO and CUR 226 UL and about 68 % in the case of CUR 226 IL. Inverse load is recommended by the CUR 226 regulation in the case of subsoil with very low bearing capacity, which is in agreement with the output of the experiment.

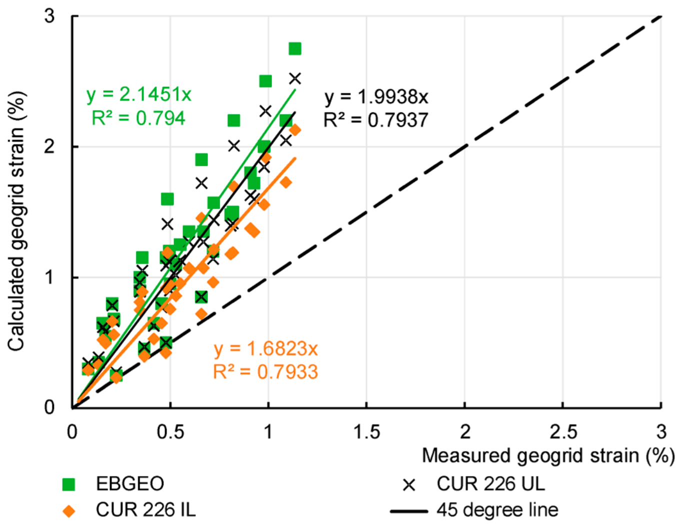

Figure 19. Regression analysis of the geogrid strain calculated using analytical methods.

Considering the negative long-term effect of rheological processes in the embankment fill and reinforcement such as consolidation, change of moisture of the fill or subsoil and creep, the difference between measured and calculated values can be a safe zone. Consolidation or moisture changes influence the stress redistribution in the embankment body while the creep process in the reinforcement affects the stiffness and the resulting forces [55]. For force calculations, a short-term geogrid stiffness was used because of the short-term nature of physical modelling. It should be also noted that maximum reinforcement strain in other studies was observed at the pile caps, and experimental results may then be closer to the predicted values [12,13,56].

5. Conclusions

Widely adopted analytical design procedures were analyzed: Marston's formula and the Hewlett and Randolph method contained in the British standard BS 8006-1, the German regulation EBGEO and the Dutch regulation CUR 226. Using these recommendations, the theoretical values of the individual parts of the load acting in the embankment and, subsequently, the values of the axial strain or tensile forces in the reinforcement were determined and compared with experimental data obtained from testy in the large-scale physical model. Monitoring of real structures can be time-consuming and some boundary conditions cannot always be fully controlled. Therefore, the utilization of large-scale physical modelling allows investigation of the piled embankment behavior at controlled conditions with the possibility to focus on partial problems. In this case, the physical model was restricted to the central part of the embankment with cohesionless fill and given geometric characteristics.

Installation of the reinforcement simulated an "infinite" strip of the geogrid with a virtual overlap outside the model boundaries. Unlike some studies with the free placement of the reinforcement on the pile caps, rigid attachment of the geogrid at the model boundaries was proven as a correct approach to simulate the continuation of the reinforcement outside the model of the central part of the embankment. Tests also proved the applicability of the strain gauges based on the optical fibers' technology allowing the investigation of the strain process of the geosynthetic reinforcement without affecting the reinforcement.

Unlike BS 8006-1 standard, the subsoil reaction and geogrid stiffness enter into the calculation in the EBGEO and CUR 226 regulations. For the presented case, without subsoil support, CUR 226 with the inverse load, which is recommended in the case of subsoil with low bearing capacity, shows a better coincidence with the measured data. Overall, EBGEO and CUR 226 can be considered to be closer to the real behavior of the piled embankment, but, especially in the case of reinforcement strain, there is a larger deviation of analytical predictions. If we assume the relaxation of the geosynthetic reinforcement and consolidation effect of the fill, we assume that the experimental outputs should probably show strains to the extent predicted by the analytical methods.

Because of the frequent utilization of geosynthetic reinforcement and possible changes of subsoil parameters during the service life of the piled embankment, a rheological process of its elements should be investigated during the design process. This can be more obvious in the case of the cohesive fill when the arching effect can also develop in a different manner, depending on the fill characteristics and preparation.

Author Contributions: Conceptualization, M.D. and J.V.; methodology, J.V.; software, J.M.; validation, J.V., F.G. and J.M.; formal analysis, M.D.; investigation, J.M.; resources, F.G.; data curation, J.V.; writing—original draft preparation, J.V.; writing—review and editing, M.D.; visualization, J.V.; supervision, M.D.; project administration, M.D.; funding acquisition, F.G. All authors have read and agreed to the published version of the manuscript.

Funding: This research was funded by Operational Programme Integrated Infrastructure: application of innovative technologies focused on the interaction of engineering constructions of transport infrastructure and the geological environment, ITMS2014+ code 313011BWS1, the project is co-funded by the European Regional Development Fund. This research was also funded by the Ministry of Education, Science, Research and Sport of the Slovak Republic, grant number VEGA 1/0484/20 "Experimental and numerical analysis of base layers of foam concrete reinforced with geosynthetics".

Data Availability Statement: Due to the nature of this research, participants of this study did not agree for their data to be shared publicly and are only available upon reasonable request.

Conflicts of Interest: The authors declare no conflict of interest.

References

1. Marschalko, M.; Zięba, Z.; Niemiec, D.; Neuman, D.; Mońka, J.; Dąbrowska, J. Suitability of engineering-geological environment on the basis of its permeability coefficient: Four case studies of fine-grained soils. *Materials* **2021**, *14*, 6411. [CrossRef] [PubMed]
2. Popielarczyk, D.; Marschalko, M.; Templin, T.; Niemiec, D.; Yilmaz, I.; Matuszková, B. Bathymetric monitoring of alluvial river bottom changes for purposes of stability of water power plant structure with a new methodology for river bottom hazard mapping (Wloclawek, Poland). *Sensors* **2020**, *20*, 5004. [CrossRef] [PubMed]
3. Slávik, I. Stability analysis of the impoundment of ash. *Slovak J. Civ. Eng.* **2013**, *21*, 17–23. [CrossRef]
4. Kortiš, J.; Daniel, L'.; Farbák, M.; Maliar, L.; Škarupa, M. Operational modal analysis of the cablestayed footbridge. *Civ. Environ. Eng.* **2017**, *13*, 92–98. [CrossRef]
5. Prokop, J.; Odrobiňák, J.; Farbák, M.; Novotný, V. Load-carrying capacity of bailey bridge in civil applications. *Appl. Sci.* **2022**, *12*, 3788. [CrossRef]
6. Sedivy, S.; Mikulova, L.; Danisovic, P.; Sramek, J.; Remek, L.; Kozel, M. Long-term monitored road degradation functions as a tool to increase quality of pavement design. *Appl. Sci.* **2021**, *11*, 9839. [CrossRef]
7. Šestáková, J.; Ižvolt, L.; Mečár, M. Degradation—prediction models of the railway track quality. *Civ. Environ. Eng.* **2019**, *15*, 115–124. [CrossRef]
8. Prelovský, B.; Naughton, P.J.; Scotto, M.; Kempton, G.T. The Development of Piled Embankments Techniques over 25 Years. In Proceedings of the Zakládání Staveb Brno, Brno, Czech Republic, 10–11 November 2008.
9. McNulty, J.W. *An Experimental Study of Arching in Sand*; Technical Report No. I–674; U.S. Army Engineer Waterways Experiment Station, Corps of Engineers: Vicksburg, MS, USA, 1965.
10. Rui, R.; van Eekelen, S.J.M.; Wan, Y. Experimental investigation of soil–arching development in unreinforced and geosynthetic-reinforced pile-supported embankments. *J. Geotech. Geoenvironmental Eng.* **2019**, *145*, 04018103. [CrossRef]
11. Stacho, J.; Sulovska, M. Numerical modelling of the subsoil zone between stone columns. *Slovak J. Civ. Eng.* **2019**, *27*, 32–39. [CrossRef]
12. Filz, G.M.; Sloan, J.A.; McGuire, M.P.; Smith, M.; Collin, J. Settlement and vertical load transfer in column-supported embankments. *J. Geotech. Geoenviron. Eng.* **2019**, *145*, 04019083. [CrossRef]
13. Van Eekelen, S.J.M.; Bezuijen, A.; Lodder, H.J.; van Tol, A.F. Model experiments on piled embankments. Part I. *Geotext. Geomembr.* **2012**, *32*, 69–81. [CrossRef]
14. Van Eekelen, S.J.M.; Bezuijen, A.; Lodder, H.J.; van Tol, A.F. Model experiments on piled embankments. Part II. *Geotext. Geomembr.* **2012**, *32*, 82–94. [CrossRef]
15. Van Eekelen, S.J.M.; Bezuijen, A.; van Tol, A.F. Validation of analytical models for the design of basal reinforced piled embankments. *Geotext. Geomembr.* **2015**, *43*, 56–81. [CrossRef]
16. Nguyen, G.; Nguyen, G. Laboratory study of soil shear strength improvement with polyester fibres. *Fibres Text. East. Eur.* **2019**, *27*, 90–99. [CrossRef]
17. *BS 8006-1*; Code of Practice for Strengthened/Reinforced Soils and Other Fills. BSI: London, UK, 2010.
18. Deutsche Gesellschaft für Geotechnik e.V. (Ed.) *Recommendations for Design and Analysis of Earth Structures Using Geosynthetic Reinforcements—EBGEO*, 2nd ed.; Ernst & Sohn Verlag: Berlin, Germany, 2010.
19. Russell, D.; Pierpoint, N. An assessment of design methods for piled embankments. *Ground Eng.* **1997**, *30*, 39–44.
20. Van Eekelen, S.J.M.; Brugman, M.H.A. *Design Guideline Basal Reinforced Piled Embankments*, 1st ed.; CRC Press: Delft, The Netherland, 2016.
21. Festag, G.; Katzenbach, R. Material Behavior of Dry Sand under Cyclic Loading. In Proceedings of the Fifteenth International Conference on Soil Mechanics and Geotechnical Engineering, Istanbul, Turkey, 27–31 August 2001.
22. Van Eekelen, S.J.M.; Van, M.A.; Bezuijen, A. The Kyoto Road, a Full-Scale Test, Measurements and Calculations. In Proceedings of the Fourteenth European Conference on Soil Mechanics and Geotechnical Engineering, Madrid, Spain, 23–28 September 2007.
23. Guido, V.A.; Kneuppel, J.D.; Sweeny, M.A. Plate Loading Tests on Geogrid Reinforced Earth Slabs. In Proceedings of the Geosynthetics '87, New Orleans, LA, USA, 24–25 February 1987.
24. Collin, J.G. Column Supported Embankment Design Considerations. In Proceedings of the 52nd Annual Geotechnical Engineering Conference, Minneapolis, MN, USA, 27 February 2004.
25. Spangler, M.G.; Handy, R.L. *Soil Engineering*, 3rd ed.; Harper and Row: New York, NY, USA, 1973.
26. John, N.W.M. *Geotextiles*, 1st ed.; Chapman and Hall: Glasgow, KY, USA, 1987.
27. Hewlett, W.J.; Randolph, M.F. Analysis of piled embankments. *Ground Eng.* **1988**, *21*, 12–18.
28. Zaeske, D. Zur Wirkungsweise von Unbewehrten und Bewehrten Mineralischen Tragschichten über Pfahlartigen Gründungselemente. Ph.D. Dissertation, University of Kassel, Kassel, Germany, 2001. (In German).
29. Van Eekelen, S.J.M.; Bezuijen, A.; van Tol, A.F. An analytical model for arching in piled embankments. *Geotext. Geomembr.* **2013**, *39*, 78–102. [CrossRef]
30. Van Eekelen, S.J.M. Basal Reinforced Piled Embankments. Ph.D. Dissertation, TU Delft, Delft, The Netherlands, 2015.
31. Lu, W.; Miao, L.; Wang, F.; Zhang, J.; Zhang, Y.; Wang, H. A case study on geogrid–reinforced and pile–supported widened highway embankment. *Geosynth. Int.* **2020**, *27*, 261–274. [CrossRef]
32. Lee, T.; van Eekelen, S.J.M.; Jung, Y.H. Numerical verification of the concentric arches model for geosynthetic–reinforced pile–supported embankments: Applicability and limitations. *Can. Geotech. J.* **2020**, *58*, 441–454. [CrossRef]

33. Satibi, S.; Leoni, M.; Vermeer, P.A. On the Numerical Analysis of Piled Embankments. In Proceedings of the Second International Workshop on Geotechnics of Soft Soils, Glasgow, UK, 3–5 September 2008.
34. Van der Peet, T.C.; van Eekelen, S.J.M. 3D Numerical Analysis of Basal Reinforced Piled Embankments. In Proceedings of the 10th International Conference on Geosynthetics–10th ICG, Berlin, Germany, 21–26 September 2014.
35. Drusa, M.; Kais, L.; Bulko, R. 3D approach of arching effect in basal reinforcement layer. *Procedia Eng.* **2014**, *91*, 352–357. [CrossRef]
36. Drusa, M.; Kais, L.; Vlček, J.; Mečár, M. Piled embankment design comparison. *Civ. Environ. Eng.* **2015**, *11*, 76–82. [CrossRef]
37. Cui, J.; Yang, Z.; Azzam, R. Field measurement and numerical study on the effects of under-excavation and over-excavation on ultra-deep foundation pit in coastal area. *J. Mar. Sci. Eng.* **2023**, *11*, 219. [CrossRef]
38. Ižvolt, L.; Dobeš, P. Measurements result analysis of deformation characteristics of transition zones on the modernized line Púchov—Považská Teplá. *Civ. Environ. Eng.* **2021**, *17*, 353–360. [CrossRef]
39. Ižvolt, L.; Dobeš, P.; Pitoňák, M. Preliminary results and conclusions from the experimental monitoring of thermal regime of railway track structure. *Int. J. Transp. Dev. Integr.* **2017**, *1*, 529–539. [CrossRef]
40. Bednarski, Ł.; Sieńko, R.; Kanty, P.; Howiacki, T. New hydraulic sensor for distributed and automated displacement measurements with temperature compensation system. *Sensors* **2021**, *21*, 4678. [CrossRef]
41. Carri, A.; Valletta, A.; Cavalca, E.; Savi, R.; Segalini, A. Advantages of IoT-based geotechnical monitoring systems integrating automatic procedures for data acquisition and elaboration. *Sensors* **2021**, *21*, 2249. [CrossRef]
42. Cviklovič, V.; Mojžiš, M.; Majdan, R.; Kollárová, K.; Tkáč, Z.; Abrahám, R.; Masarovičová, S. Data acquisition system for on-the-go soil resistance force sensor using soil cutting blades. *Sensors* **2022**, *22*, 5301. [CrossRef]
43. Valletta, A.; Carri, A.; Segalini, A. Alert threshold assessment based on equivalent displacements for the identification of potentially critical landslide events. *Nat. Hazards* **2023**, *115*, 1549–1570. [CrossRef]
44. Den Boogert, T.J.M. Piled Embankments with Geosynthetic Reinforcement, Numerical Analysis of Scale Model Tests. Master's Thesis, Delft University of Technology, Delft, The Netherlands, 2011.
45. *ISO 10319*; Geosynthetics–Wide-Width Tensile Test. International Organization for Standardization: Geneva, Switzerland, 2015.
46. Lee, T.; Lee, S.H.; Lee, I.W.; Jung, Y.H. Lessons from full–scale experiments on piled embankments with different geosynthetic reinforcements. *KSCE J. Civ. Eng.* **2021**, *25*, 442–450. [CrossRef]
47. Stacho, J.; Sulovska, M.; Slavik, I. Determining the shear strength properties of a soil-geogrid interface using a large-scale direct shear test apparatus. *Period. Polytech. Civ. Eng.* **2020**, *64*, 989–998. [CrossRef]
48. Heitz, C. Bodengewölbe unter ruhender und nichtruhender Belastung bei Berücksichtigung von Bewehrungseinlagen aus Geogittern. Ph.D. Dissertation, University of Kassel, Kassel, Germany, 2006. (In German).
49. Drusa, M.; Kais, L.; Dubovan, J.; Markovič, M.; Bahleda, F.; Mečár, M. Measurement of axial strain of geogrid by optical sensors. *Sensors* **2021**, *21*, 6404. [CrossRef] [PubMed]
50. Kempfert, H.G.; Göbel, C.; Alexiew, D.; Heitz, C. German Recommendations for Reinforced Embankments on Pile–Similar Elements. In Proceedings of the EuroGeo 3, Munich, Germany, 1–3 March 2004.
51. Kempfert, H.G.; Zaeske, D.; Alexiew, D. Interactions in Reinforced Bearing Layers over Partial Supported Underground. In Proceedings of the XIIth ECSME Conference, Amsterdam, The Netherlands, 7–10 June 1999.
52. Haus, J. *Optical Sensors: Basics and Applications*, 1st ed.; Wiley: Hoboken, NJ, USA, 2010.
53. Yin, S.; Ruffin, P.B.; Yu, F.T.S. *Fiber Optics Sensors*, 2nd ed.; Taylor & Francis: New York, NY, USA, 2008.
54. Han, J. Design and Construction of Embankments on Geosynthetic Reinforced Platforms Supported by Piles. In Proceedings of the ASCE/PaDOT Geotechnical Seminar, Hershey, PA, USA, 1–3 April 1999.
55. Van Eekelen, S.J.M.; Venmans, A.A.M.; Bezuijen, A.; van Tol, A.F. Long term measurements in the Woerden geosynthetic-reinforced pile-supported embankment. *Geosynth. Int.* **2020**, *27*, 142–156. [CrossRef]
56. Van der Peet, T.C. Arching in Basal Reinforced Piled Embankments. Master's Thesis, TU Delft, Delft, The Netherlands, 2014.